

Zonal and Vertical Structure of the Madden–Julian Oscillation

GEORGE N. KILADIS

NOAA/Aeronomy Laboratory, Boulder, Colorado

KATHERINE H. STRAUB

Department of Geological and Environmental Sciences, Susquehanna University, Selinsgrove, Pennsylvania

PATRICK T. HAERTEL

Department of Atmospheric Sciences, University of North Dakota, Grand Forks, North Dakota

(Manuscript received 23 September 2004, in final form 4 February 2005)

ABSTRACT

A statistical study of the three-dimensional structure of the Madden–Julian oscillation (MJO) is carried out by projecting dynamical fields from reanalysis and radiosonde data onto space–time filtered outgoing longwave radiation (OLR) data. MJO convection is generally preceded by low-level convergence and upward motion in the lower troposphere, while subsidence, cooling, and drying prevail aloft. This leads to moistening of the boundary layer and the development of shallow convection, followed by a gradual and then more rapid lofting of moisture into the middle troposphere at the onset of deep convection. After the passage of the heaviest rainfall, a westerly wind burst region is accompanied by stratiform precipitation, where lower tropospheric subsidence and drying coincide with continuing upper tropospheric upward motion. The evolution of the heating field leads to a temperature structure that favors the growth of the MJO. The analysis also reveals distinct differences in the vertical structure of the MJO as it evolves, presumably reflecting changes in its vertical heating profile, phase speed, or the basic-state circulation that the MJO propagates through.

The dynamical structure and the evolution of cloud morphology within the MJO compares favorably in many respects with other propagating convectively coupled equatorial waves. One implication is that the larger convective envelopes within the Tropics tend to be composed of more shallow convection along their leading edges, a combination of deep convection and stratiform rainfall in their centers, and then a preponderance of stratiform rainfall along their trailing edges, regardless of scale or propagation direction. While this may ultimately be the factor that governs the dynamical similarities across the various wave types, it raises questions about how the smaller-scale, higher-frequency disturbances making up the MJO conspire to produce its heating and dynamical structures. This suggests that the observed cloud morphology is dictated by fundamental interactions with the large-scale circulation.

1. Introduction

The Madden–Julian oscillation (MJO) has been the topic of numerous studies over the past three decades (see Madden and Julian 2005; Wang 2005; Zhang 2005 for detailed summaries). Despite such intensive scrutiny, a comprehensive theory for the MJO, one that accounts for its genesis, structure, and propagation

characteristics, has proven elusive. Such a theory would be required to explain, among other aspects, the mechanism for the eastward propagation of the disturbance, its spatial scale and phase speed, and the nature of the interactions with higher-frequency disturbances that make up its convective envelope. Nevertheless, much progress has been made in documenting the observed structure of the disturbance (e.g., Madden and Julian 1972; Weickmann 1983; Rui and Wang 1990; Hendon and Salby 1994; Chen et al. 1996; Lin and Johnson 1996; Houze et al. 2000; Yanai et al. 2000). General circulation model (GCM) simulations of the MJO have also shown steady improvements over the

Corresponding author address: George N. Kiladis, NOAA/Aeronomy Laboratory, R/AL3, 325 Broadway, Boulder, CO 80305-3328.

E-mail: gkiladis@al.noaa.gov

years (Hayashi and Golder 1993; Sperber et al. 1997; Wang and Schlesinger 1999; Inness and Slingo 2003) and mesoscale models are currently improving the regional aspects of MJO simulations (Gustafson and Weare 2004).

Diagnosis of the dynamical mechanisms at work in GCMs is still formidable, even if the models realistically simulate the MJO. One very useful alternative avenue has been provided by simple dynamical models, where many of the complexities of GCMs are stripped away by using fewer vertical levels and/or simplified physics (e.g., Lau and Peng 1987; Chao 1987; Hendon 1988; Chang and Lim 1988; Wang and Chen 1989; Bladé and Hartmann 1993; Salby et al. 1994; Neelin and Yu 1994; Lin et al. 2000; Lindzen 2003). Such studies have attempted to identify mechanisms responsible for the coupling of convection to the large-scale MJO circulation, while other simulations have provided insight into the potential roles of air–sea interaction (e.g., Emanuel 1987; Neelin et al. 1987) and cloud-radiation feedback (Hu and Randall 1994; Raymond 2001) in the MJO.

Despite the progress made in understanding some of the fundamental mechanisms key to MJO dynamics, few theoretical or modeling studies thus far have attempted to account for the effects of scale interactions between the MJO and other disturbances (Meehl et al. 2001). It is now well known that the MJO convective envelope is composed of a host of higher-frequency modes propagating both eastward and westward (e.g., Nakazawa 1988; Mapes and Houze 1993; Hendon and Liebmann 1994; Dunkerton and Crum 1995). Although much of this activity is organized on the mesoscale, many of these disturbances can be identified as synoptic-scale convectively coupled equatorial waves, having the dispersion characteristics and structures of the normal modes of the linearized shallow water equations on an equatorial beta plane (Takayabu 1994; Wheeler and Kiladis 1999, hereafter WK99; Wheeler et al. 2000). These modes include Kelvin, equatorial Rossby (ER), mixed Rossby–gravity (MRG), and westward inertia-gravity (WIG) waves.

Straub and Kiladis (2003a) showed that the number of westward propagating MRG and easterly waves, along with tropical depressions, is increased within the MJO convective region over the western Pacific. The MJO also modulates Kelvin wave activity (eastward propagating superclusters) within its envelope over the Indian Ocean, but well to the east of its location once it propagates into the western Pacific. In addition, Roundy and Frank (2004a,b) have shown that the MJO cooperatively interacts with westward propagating ER modes, which may be important for MJO amplification

or genesis. There is also evidence that Kelvin waves are at times implicated in the initiation of a northward propagating MJO associated with monsoon onset over India (Flatau et al. 2003). These observations suggest that successful modeling of the MJO will ultimately depend on the simulation of interactions between the MJO and these higher-frequency, smaller-scale disturbances (Krishnamurti et al. 2003). Recent efforts to represent such scale interactions in simple models (e.g., Moncrieff 2004; Majda and Biello 2004; Biello and Majda 2005), and in numerical superparameterization settings with cloud-resolving simulations embedded within larger scale models (e.g., Grabowski 2003; Randall et al. 2003), have shown encouragingly realistic results.

Several recent studies have examined the large-scale vertical structure of the MJO using various statistical approaches (Kemball-Cook and Weare 2001; Sperber 2003; Lin et al. 2004). These results have revealed that the MJO displays some features in common with other synoptic-scale convective disturbances in the Tropics. The present study examines the temporal evolution and zonal/vertical structure of the MJO, focusing in particular on differences in its properties as it propagates from the western Indian Ocean to the central Pacific. This structure is compared with that of other equatorial waves described by Wheeler et al. (2000). One goal is to provide targets for the simulation of the MJO in GCMs and simpler dynamical models. We also aim to provide some observational basis for the relationship between the MJO and the higher-frequency disturbances composing, which ultimately will have to be assessed and accounted for through theory and modeling.

2. Data and methodology

The primary index used here to identify MJO convection is based on the interpolated outgoing longwave radiation (OLR) dataset (Liebmann and Smith 1996). Both European Centre for Medium-Range Weather Forecasts (ECMWF) 15-yr Re-analysis (ERA-15) and National Centers for Environmental Prediction (NCEP) reanalysis data were used as sources for the dynamical fields in this study. These data are supplemented by quality-controlled radiosonde observations of wind, temperature, geopotential height, and humidity from several tropical stations in the comprehensive aerological reference dataset (CARDS), obtained from the National Oceanic and Atmospheric Administration (NOAA)/National Climatic Data Center (NCDC). The vertical resolution varies, but the radiosonde data are usually stored at 15 mandatory pressure levels from 1000 to 10 hPa, and in some cases as many as 29 levels with 50-hPa vertical resolution are available. While the

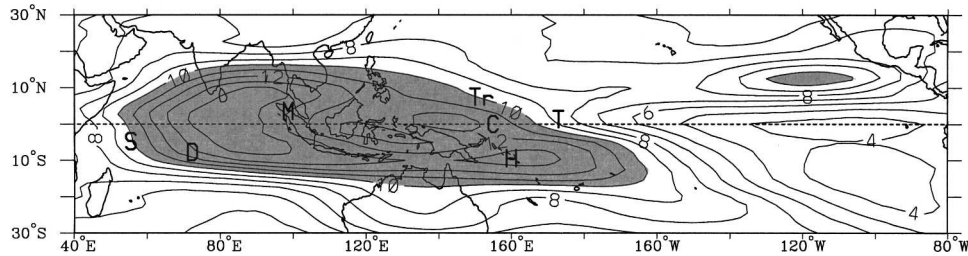


FIG. 1. Daily standard deviation of MJO-filtered OLR (see text) for the period 1979–2004. Contour interval is 1 W m^{-2} . Shading denotes standard deviations greater than 10 W m^{-2} . Also shown are the locations of the TOGA COARE base point used in the analysis (denoted C, at equator, 155°E) and radiosonde stations Seychelles (“S,” 4.7°S , 55.5°E), Diego Garcia (“D,” 7.7°S , 72.4°E), Medan (“M,” 3.6°N , 98.7°E), Honiara (“H,” 9.4°S , 160.0°E), Truk (“Tr,” 7.5°N , 151.9°E), and Tarawa (“T,” 1.4°N , 172.9°E).

reanalysis data effectively capture the large-scale features of the MJO, the use of radiosonde data is crucial for isolating more subtle details that may be important to the dynamics.

There have been many efforts to derive indices of the MJO in the literature. Temporal filtering (e.g., Weickmann et al. 1985; Kiladis and Weickmann 1992), EOF analyses of wind or OLR (Weickmann 1983; Hendon et al. 1999; Kessler 2001; Matthews 2000; Wheeler and Hendon 2004), and singular value decomposition (e.g., Weare 2003) are typical approaches. For our purposes an index is obtained as in WK99 by space–time filtering OLR to retain only eastward propagating signals of wavenumbers 0–9 with periods between 30 and 96 days. This filter differs from that of WK99 in that they only considered eastward waves 1–5 in their analysis, whereas zonal mean signals of the MJO are substantial (e.g., Weickmann et al. 1997) and the higher wavenumber components that are now included stand above the background in WK99. Our results were checked against a variety of other MJO indices. Results using any reasonable index differ only in details that do not change any conclusions drawn in this paper. The space–time filtering approach used here is particularly suitable for examining lagged signals in station data at a particular location, where the use of one number as an index is convenient. Figure 1 shows the daily standard deviation of the MJO index for the period 1979–2004. As noted in many previous studies, the MJO is most active over the warm pool regions of high mean sea surface temperature (SST) of the tropical Indian and west Pacific Oceans.

The MJO index is correlated and regressed against dynamical fields or OLR to obtain a composite picture of MJO evolution, using the technique outlined by Wheeler et al. (2000). For all of the plots in this paper, the perturbations are scaled to a -40 W m^{-2} OLR anomaly, a typical minimum value seen during the pas-

sage of a moderately strong MJO. We initially stratified our analysis seasonally, and found that some differences in structure do exist, especially during the solstice seasons (e.g., Kemball-Cook and Wang 2001; Zhang and Dong 2004). In this paper, we focus primarily on signals when MJO convective activity is near the equator, where seasonal differences were found to be minimal (as was also found by Lin et al. 2005), so for this study statistics were derived using data from all seasons. The reanalysis results shown here are representative of a point near the center of the Tropical Ocean Global Atmosphere Coupled Ocean–Atmosphere Response Experiment (TOGA COARE) intensive flux array (equator, 155°E , denoted C in Fig. 1), for comparison with results from that field experiment. For radiosonde data, the basis is MJO-filtered OLR at the grid point closest to the station. Out of more than 25 high quality radiosonde records examined, we chose to present the results from the locations shown in Fig. 1, since they are representative of the regional differences emphasized in this study. Features discussed in this paper are all statistically significant at better than the 95% level, after taking into account temporal autocorrelation, and every figure shown is field significant according to the criteria outlined in Livezey and Chen (1983).

We first describe the observational results. This will be followed by an interpretation and comparison with other convectively coupled equatorial waves, and a discussion of some remaining unresolved issues.

3. Observational results

a. Horizontal circulation

Figure 2 illustrates the regressed day 0 OLR and flow fields at 200 and 850 hPa using the MJO-filtered OLR at the COARE base point, and provides a large-scale

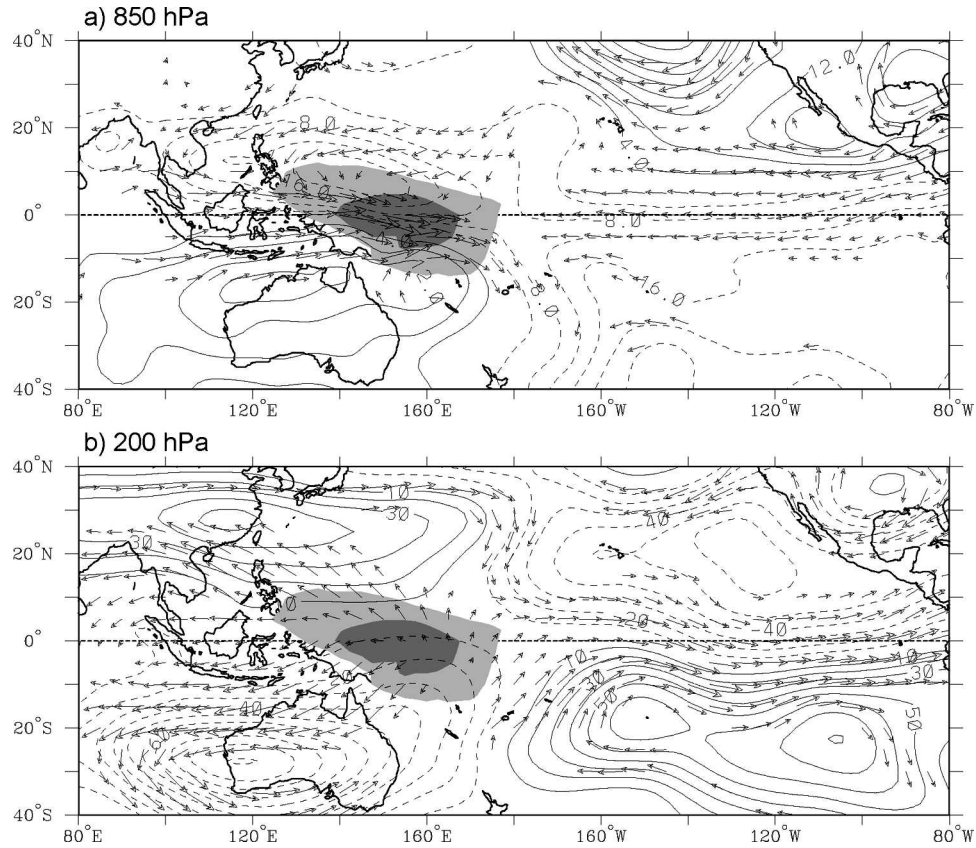


FIG. 2. Anomalous OLR and circulation from ERA-15 reanalysis on day 0 associated with a -40 W m^{-2} perturbation in MJO-filtered OLR at the equator, 155°E for the period 1979–93, all seasons included; (a) 850 and (b) 200 hPa. Dark (light) shading denotes OLR anomalies less than -32 W m^{-2} (-16 W m^{-2}). Streamfunction contour interval is (a) $4 \times 10^5 \text{ m}^2 \text{ s}^{-1}$ and (b) $10 \times 10^5 \text{ m}^2 \text{ s}^{-1}$. Locally statistically significant wind vectors at the 95% level are shown. The largest vectors are about 2 m s^{-1} in (a) and around 5 m s^{-1} in (b).

context for the results to follow. Figure 2 is quite similar to patterns obtained by Weickmann (1983), Hendon and Salby (1994), and many subsequent studies using various methods. At 850 hPa (Fig. 2a), a familiar pattern of cyclonic Rossby gyres flanks the convective region, with a broad fetch of equatorial easterlies present over the Pacific. These easterlies connect all the way around to the western Indian Ocean, as shown below. Westerly flow extends through and to the east of the OLR minimum, and reaches maximum amplitude to the west of the OLR minimum over Indonesia. The details of this westerly wind burst (WWB) feature have been discussed extensively in many previous studies (e.g., Rui and Wang 1990; Hendon and Salby 1994; Kiladis et al. 1994). Little change in the circulation is seen at levels below 850 hPa (not shown), apart from a lower amplitude and a slight eastward displacement. The entire pattern is generally interpreted as a forced Rossby–Kelvin response to the convective heating (e.g.,

Lau and Peng 1987; Salby et al. 1994; Houze et al. 2000; Matthews et al. 2004).

The corresponding pattern at 200 hPa (Fig. 2b) displays significant divergent (cross streamfunction) outflow surrounding the convection, with subtropical anticyclonic flow anomalies over the Indian sector and Pacific cyclones completing a quadrupole rotational circulation. Overall the 200-hPa flow features are of larger scale than the lower tropospheric flow in Fig. 2a, with the equatorial Pacific westerlies more clearly tied to Rossby gyres in the subtropics.

The planetary extent of the MJO circulation on day 0 is evident in an equatorial cross section of zonal wind anomalies (u' ; Fig. 3). The WWB is present in a deep layer from the eastern Indian Ocean to the date line, with a 700-hPa maximum centered at 140°E , 15° west of the minimum OLR perturbation. These westerlies extend up to around 300 hPa within and to the west of the vicinity of the convection, lying

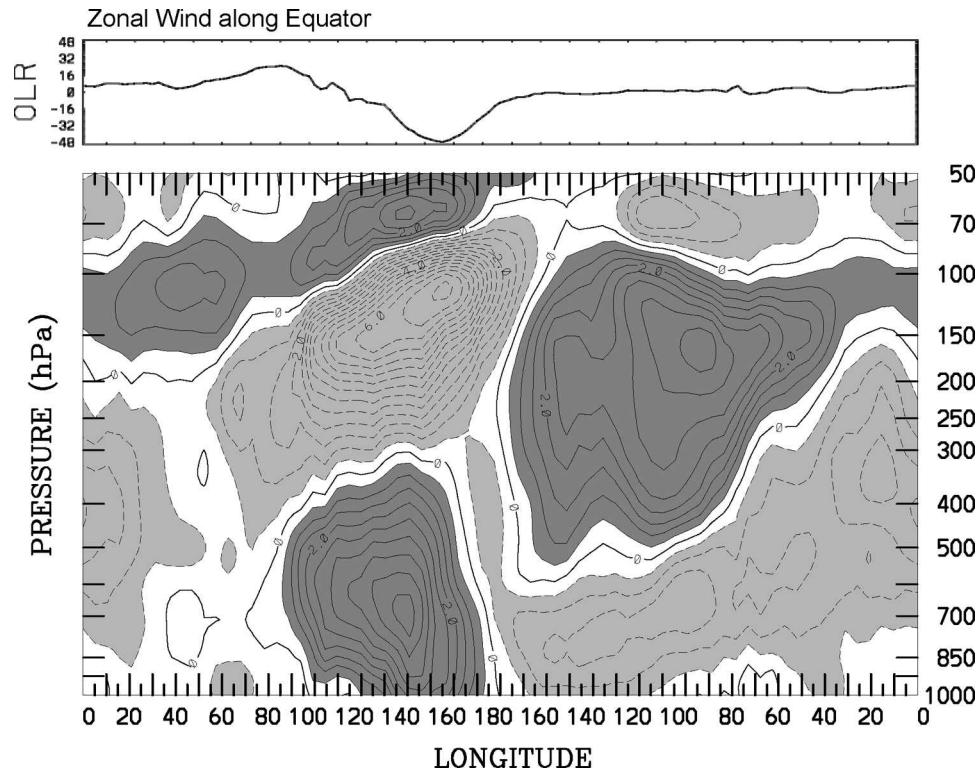


FIG. 3. Zonal/height cross section of anomalous zonal wind along the equator associated with the pattern in Fig. 2. Contour interval is 0.5 m s^{-1} ; negative contours dashed. Dark (light) shading denotes anomalies greater than (less than) $\pm 0.5 \text{ m s}^{-1}$. The associated OLR anomaly along the equator is shown at the top in W m^{-2} .

below easterly perturbations tilting upward and eastward into the stratosphere. The westward tilt with height of the WWB is in accord with observations of individual cases, where westerlies are seen first near the surface as MJO convection develops, propagating upward over time (Gutzler et al. 1994; Tung and Yanai 2002). East of the date line, strong upper tropospheric westerlies peak at 150 hPa around 100°W , extending around the globe until they tilt upward and eastward into the lower stratosphere above the convection. Beneath the upper westerlies lie weaker low-level easterlies that wrap around into the Indian Ocean.

The relationships between surface wind stress, radiation, and MJO convection are crucial elements of the potential ocean–atmosphere interactions associated with the oscillation. Zhang and McPhaden (2000) and Zhang and Anderson (2003) review the range of possible phasings, and conclude from observational evidence that surface westerlies generally lie within the MJO convective region (their Model II) although in some cases, as over the Indian Ocean, convection is found closer to the boundary between westerlies and easterlies (Model I). This transition was also confirmed

by Sperber (2003). This geographical dependence of MJO zonal wind behavior is also seen in radiosonde observations in Fig. 4. In all radiosonde plots, time is plotted from right to left for easier comparison with zonal cross sections, and the corresponding OLR perturbation values at the grid point nearest to the station are also given for each lag. Figure 4a from Diego Garcia represents the typical signal over the Indian Ocean and is very similar to other open ocean locations west of Australasia (e.g., Seychelles and Cocos Island at 12.2°S , 96.8°E ; not shown). At Diego Garcia, MJO convection is preceded by low-level easterly and upper tropospheric westerly anomalies, giving way over time to opposite-signed signals just prior to the OLR minimum. In the lower troposphere, these show little vertical tilt, with u' building vertically nearly simultaneously, and lower (upper) tropospheric easterlies (westerlies) peaking at 850 hPa around day -14 and somewhat stronger opposite signed signals at day $+10$. Here anomalous surface westerlies are displaced only slightly into the region of peak convection. Similar results were obtained using both NCEP and ERA-15 reanalyses by Sperber (2003) and Lin et al. (2005).

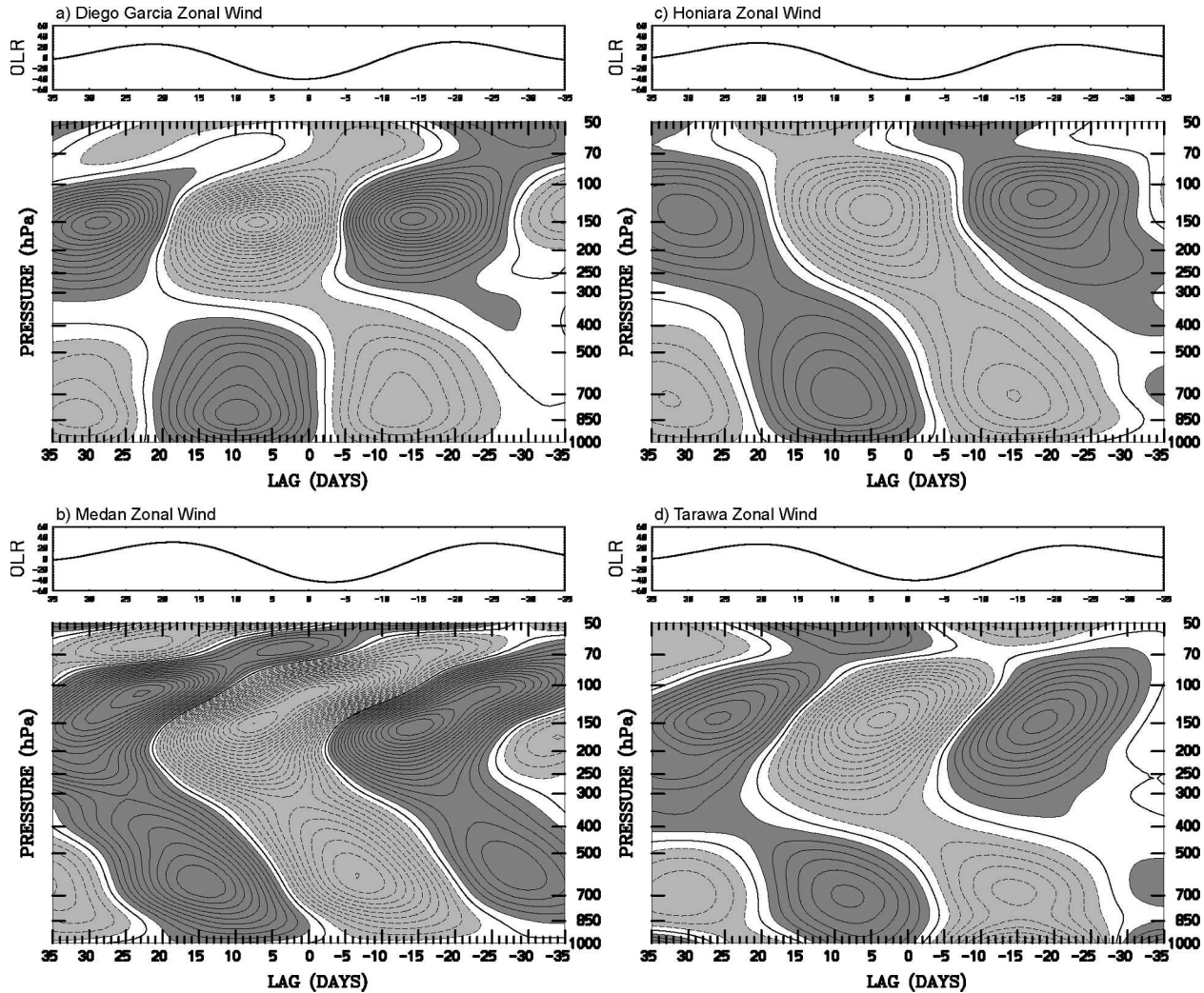


FIG. 4. Time-height cross section of the zonal wind anomaly at (a) Diego Garcia, (b) Medan, (c) Honiara, and (d) Tarawa, scaled to a -40 W m^{-2} perturbation in MJO-filtered OLR at the nearest grid point to each station. Contour interval is 0.5 m s^{-1} ; negative contours dashed. Dark (light) shading denotes anomalies greater than (less than) $\pm 0.5 \text{ m s}^{-1}$. The associated OLR anomaly is shown at the top in W m^{-2} .

Contrasting behavior over Indonesia and the western Pacific is illustrated by Fig. 4b at Medan, and at Honiara, south of the COARE region (Fig. 4c). At these locations the low-level zonal wind moves upward over time, rather than being a more discreet two-signed vertical structure as at Diego Garcia. Also, the westerlies show a maximum at either 600 or 700 hPa instead of 850 hPa, and are about 50% stronger for a given OLR perturbation at Medan. Based on the full sample of radiosonde results, this higher amplitude signal does not appear to be the result of distance from the equator, but is also present at other Indonesian locations (not shown). It is, however, not well reproduced in reanalysis, and may be due to a greater intensity of land-based convection. Just west of the date line at Tarawa

(Fig. 4d) there are strong easterlies within the boundary layer ahead of the MJO, a signal that is not captured well in the set of lagged ERA-15 plots such as Figs. 2a and 3 (not shown). Here the westerlies extend slightly farther into the region of convection than at sites over the Indian Ocean, although the phasing is still not as extreme as Model II of Zhang and McPhaden (2000), which would have maximum surface westerlies coincident with deepest convection. The Tarawa zonal wind profile also begins to tilt upward and eastward above 400 hPa, much lower than at the stations farther west and a feature common to other stations east of 160°E (not shown). The origin of this difference is not immediately clear, although we note that the easterly shear of the basic state with height begins to decrease east of the

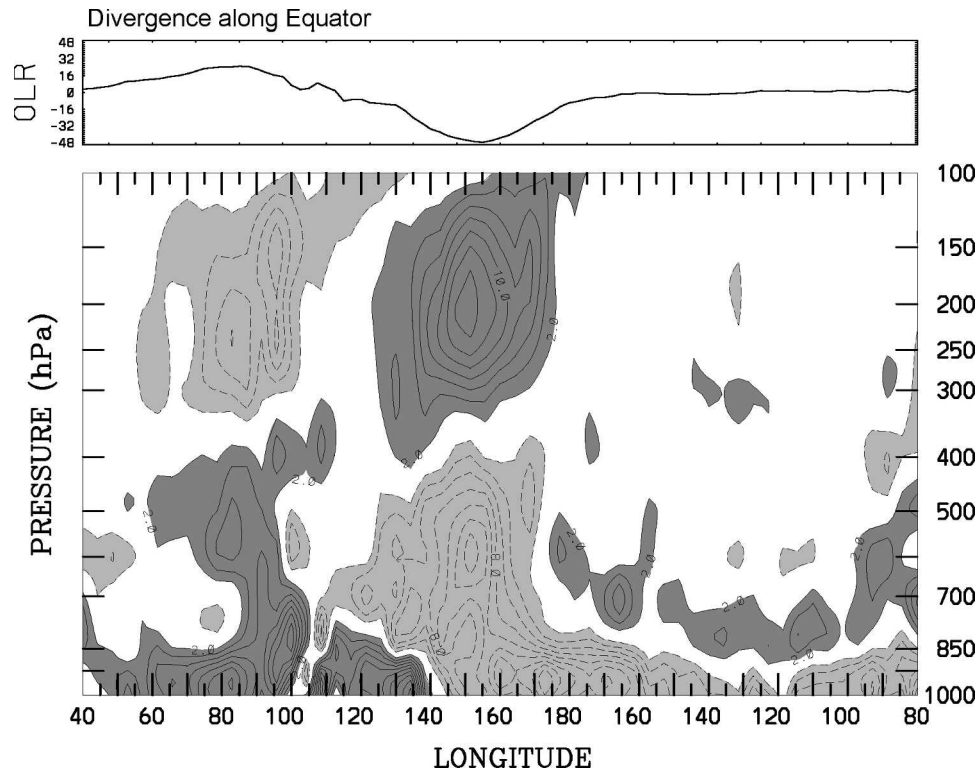


FIG. 5. As in Fig. 3, except for mass divergence $(\rho \nabla \cdot \mathbf{V})'$ along the equator from 40°E to 80°W. Contour interval is $2 \times 10^{-7} \text{ kg m}^{-3} \text{ s}^{-1}$.

warm pool, which may favor the trapping of equatorial wave kinetic energy in the upper troposphere (Wang and Xie 1996).

b. Divergence

Rui and Wang (1990), Hendon and Salby (1994), Zhang (1996), Jones and Weare (1996), Maloney and Hartmann (1998), and Hsu et al. (2004), among others, found evidence of low-level convergence leading MJO convection as it propagated eastward, and pronounced vertical tilts in divergence. Figure 5 is a zonal cross section of the anomalous mass divergence $(\rho \nabla \cdot \mathbf{V})'$ computed using centered differences. This field has also been partitioned into zonal $(\rho \partial u / \partial x)'$ and meridional $(\rho \partial v / \partial y)'$ components (not shown), and they are broadly representative of the vertical mass divergence field at various other locations during the MJO life cycle. We note that these patterns are quite similar using NCEP reanalysis, so any dependence on first-guess model parameterizations are at least consistent between the two reanalyses.

In Fig. 5, a broad region of near-surface convergence extends far to the east of the date line, and is weakest and most shallow at 120°W. This convergence is domi-

nated by the meridional flux as would be expected from the cross-isobaric flow due to frictional effects in the Kelvin response region (see Wang 1988; Salby et al. 1994; Maloney and Hartmann 1998; Moskowicz and Bretherton 2000; Seo and Kim 2003). Above this surface convergence lies a layer of anomalous divergence, consistent with a signal of detrainment by anomalous shallow convection, roughly paralleling the mean height of the trade inversion across the Pacific. To the west, the low-level convergence gradually deepens then tilts sharply upward at 170°E to fill the entire layer below 400 hPa in the convective region. Here the main convergence peak is at around 600 hPa, just below the melting level and collocated with the minimum OLR (at 155°E). This is produced almost exclusively by strong zonal convergence within the WWB region, characteristic of the midlevel inflow observed within a variety of mesoscale systems over the warm pool (Houze et al. 2000) and consistent with a top-heavy heating profile as shown by Lin et al. (2004). Divergence is aligned with the location of minimum OLR above 300 hPa, peaking at around 200 hPa. Throughout the life cycle of the MJO, this upper tropospheric divergence signal closely tracks the location of the OLR minimum (Rui and Wang 1990), and is dominated by

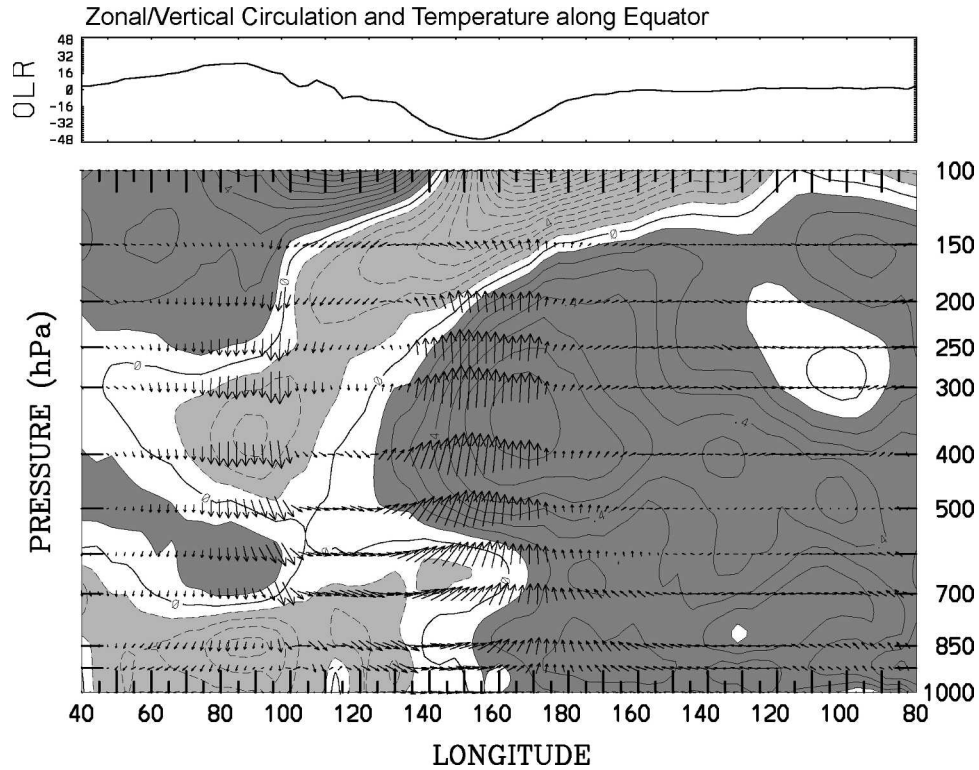


FIG. 6. As in Fig. 3, except for zonal-vertical mass flux $(\rho u, \rho w)'$ and temperature along the equator from 40°E to 80°W. Contour interval is 0.1 K. The flux $\rho w'$ has been multiplied by 1200 to account for the aspect ratio of the plot. The largest zonal flux vector is around $1 \times 10^{-3} \text{ kg m}^{-2} \text{ s}^{-1}$, and the largest vertical flux vector around $2 \times 10^{-6} \text{ kg m}^{-2} \text{ s}^{-1}$.

the meridional component of the wind (as seen, e.g., in Fig. 2b). Overall the vertical profile of divergence at 155°E in Fig. 5 is a good match to that observed within deep convection during COARE, whereas to the west the higher mode profile at 110°–140°E, with low-level divergence and elevated convergence in the midtroposphere, is more typical of stratiform regimes (Mapes and Houze 1995). In this region, the divergence within the lowest levels is due almost entirely to zonal acceleration of the westerlies into the WWB to the east.

Maps and time–longitude sections of divergence at various levels (not show) reveal that, as in Fig. 5, convergence is in phase with the minimum OLR in a deep layer from around 850 hPa up to 400 hPa, but leads by around 40°–50° longitude (roughly 8–10 days) at the surface over the Indian and west Pacific sectors (e.g., Rui and Wang 1990). Once convection decreases over the west Pacific warm pool the divergence signal weakens considerably at all levels and propagates rapidly eastward across the Pacific (see Hendon and Salby 1994, and discussion below).

c. Temperature and vertical circulation

Figure 6 shows the regressed temperature (t') and the zonal mass flux $(\rho u)'$ combined with the vertical mass flux $(\rho w)'$ along the equator. The convective region is accompanied by broad upward motion extending over roughly 60° of longitude, with downward motion of a similar scale over the eastern Indian Ocean. The upward mass flux peaks at 400 hPa and coincides with the same grid point as the minimum in OLR, as would the inferred latent heating and precipitation. At 140°–150°E there is evidence of midlevel inflow peaking at 600 hPa, as was observed in mesoscale cloud clusters by Houze et al. (2000) during COARE.

Locally around the region of minimum OLR the vertical temperature structure matches well with that observed across a wide variety of convective disturbances, with cold perturbations near the surface, between 700 and 600 hPa, and at 100 hPa, and a warm signal at 300–400 hPa (e.g., Reed et al. 1977; Gamache and Houze 1985; Sherwood and Warhlich 1999; Wheeler et al. 2000; Sherwood et al. 2003). In Fig. 6, vertically integrated tropospheric warmth occurs to the east of the

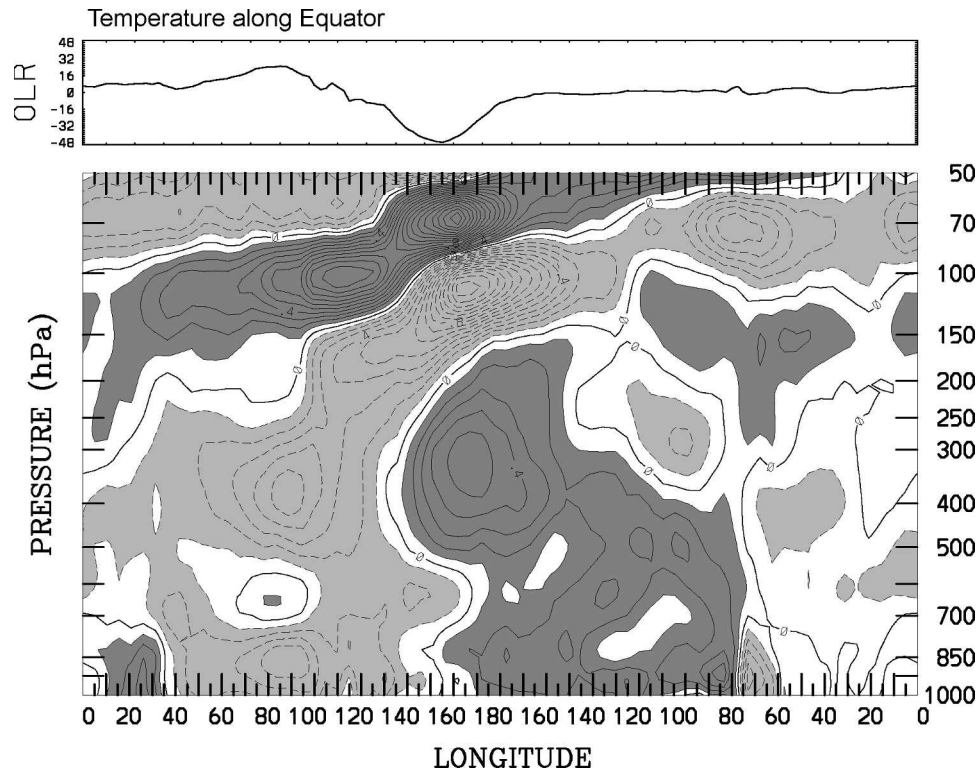


FIG. 7. As in Fig. 3, except for anomalous temperature along the equator. Contour interval is 0.1 K.

MJO, as was also documented by Salby and Hendon (1994). The largest positive t' in the midtroposphere is within and to the east of the longitude of maximum upward motion. This matches well with the signal obtained by Lin et al. (2005), although these authors found a large discrepancy between ERA-15 and NCEP reanalyses with peak t' in NCEP occurring substantially farther to the east. We have also confirmed this discrepancy using our methodology. As shown below, we find that radiosonde data are more consistent with the ERA-15 results, although the phasing between temperature and vertical motion still varies substantially with location.

Peak lower troposphere t' occurs to the east of the date line in Fig. 6. On the west side of the envelope in the midlevel inflow region there is a cold layer at 700 hPa sandwiched between warmth above and below. This signal may be partly due to evaporation within mesoscale downdrafts (e.g., Gamache and Houze 1985) as well as large-scale uplift below the level of substantial latent heating. In the region of general subsidence behind the MJO over the Indian Ocean, the lowest layers are cold. This signature is in phase with the negative SST anomaly that results from the shortwave radiation and eddy heat flux anomalies behind the MJO (Zhang 1996; Flatau et al. 1997; Shinoda et al. 1998;

Waliser et al. 1999; Woolnough et al. 2000; Maloney and Sobel 2004; Zhang 2005).

The global scale equatorial t' signal of the MJO is shown in Fig. 7. The tilted upper tropospheric t' structures of Fig. 6 are seen to be part of the large amplitude t' signals extending into the lower stratosphere, which are well-documented features of the MJO (Kiladis et al. 2001). A cold signal at tropopause level near the center of the convective envelope appears to be due in part to adiabatic lofting caused by convective heating below (Sherwood et al. 2003). This is overlain by a warm layer in the lower stratosphere. The vertical tilt of these features is consistent with the upward group velocity of a forced gravity wave response to the eastward moving MJO heat source. This interpretation is supported by the fact that the upper portion of the t' signal in westward moving equatorial waves tilts in the opposite direction (Wheeler et al. 2000; Haertel and Kiladis 2004).

As with zonal wind, there are substantial differences in the vertical structure of t' between the Indian and Indo/Pacific. Figure 8 shows the evolution of temperature during the passage of the MJO at Seychelles, Diego Garcia, Medan, and Tarawa. At all stations t' is positive on day 0 at 250 and 850 hPa, and weakly negative at the surface. There is a strong cold t' signal centered on 100 or 150 hPa and a warm signal above in the

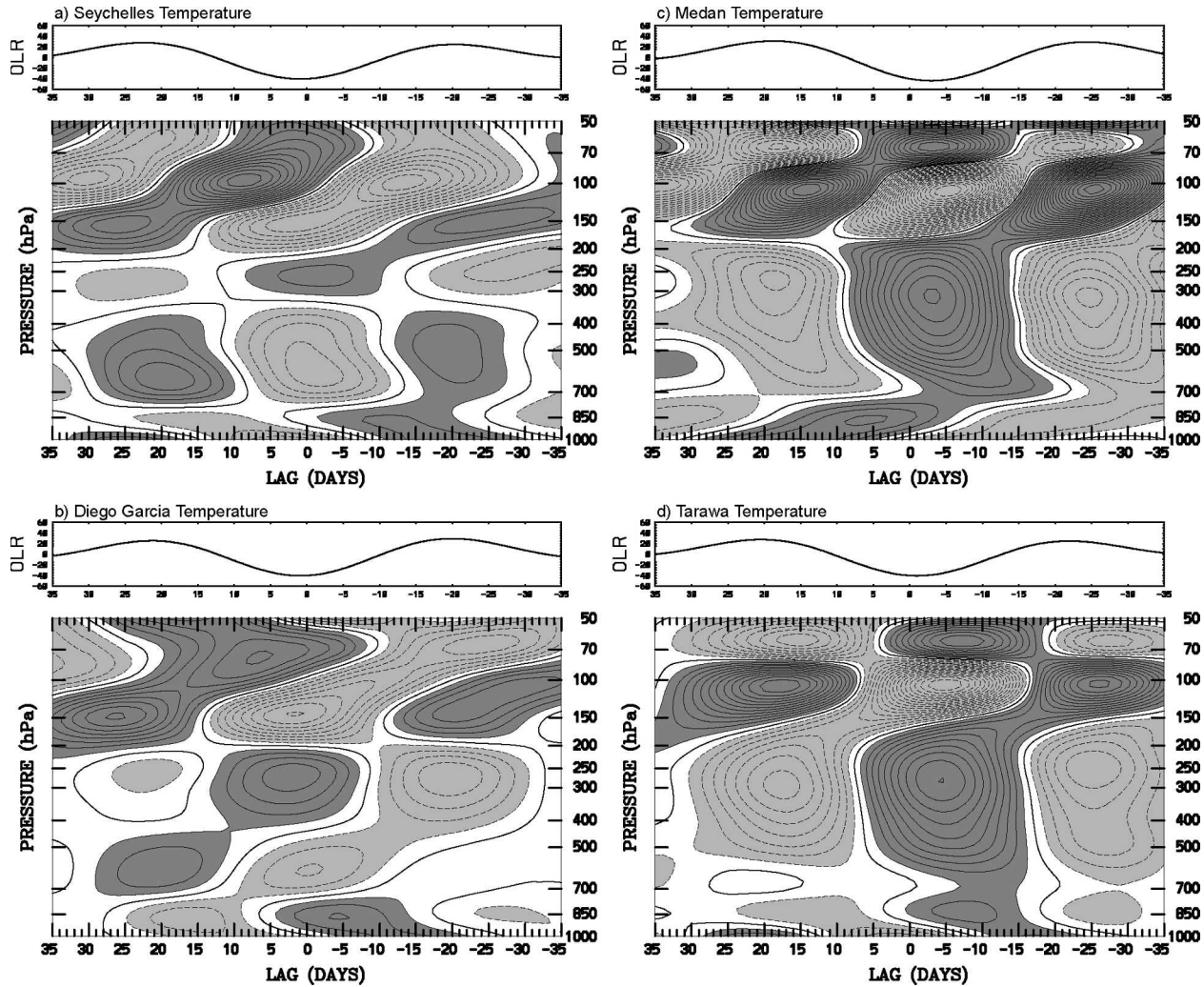


FIG. 8. As in Fig. 4, except for anomalous temperature at (a) Seychelles, (b) Diego Garcia, (c) Medan, and (d) Tarawa. Contour interval is 0.1 K.

lower stratosphere. Another cold perturbation appears between 700 and 500 hPa at Seychelles (Fig. 8a) and Diego Garcia (Fig. 8b). This higher vertical mode structure of t' is present to varying degrees at all stations, although it is manifested as only a weak negative t' or a significant local weakening of a positive perturbation at 700 hPa at sites in the Pacific and Indonesia, as in Figs. 8c and 8d.

Another feature common to the majority of especially open ocean sites is a warm signal that appears first at the surface ahead of the convection, then works its way up to the 850-hPa level. This is followed by a strengthening cold signal within the boundary layer, which may initially be due to mesoscale downdrafts as the deepest convection develops. High surface t' ahead of the MJO with low surface t' following are well-known features of the disturbance (e.g., Zhang 1996;

Sperber 2003). However, the spreading of these signals upward into the boundary layer is less well documented and will be discussed further below.

d. Specific humidity

The zonal structure of specific humidity anomalies (q') associated with the MJO from reanalysis is shown in Fig. 9. This plot only extends to the 300-hPa level, which is considered to be the maximum height of useful humidity data from reanalysis and radiosondes. Satellite observations reveal that the MJO transports moisture into the upper troposphere and lower stratosphere, nearly in phase with the upper tropospheric q' signals shown here (e.g., Mote et al. 2000; Sassi et al. 2002). Plots of q' can also be treated as close proxies for perturbation moist static energy, which look quite similar.

To the east of the MJO convective center, over the

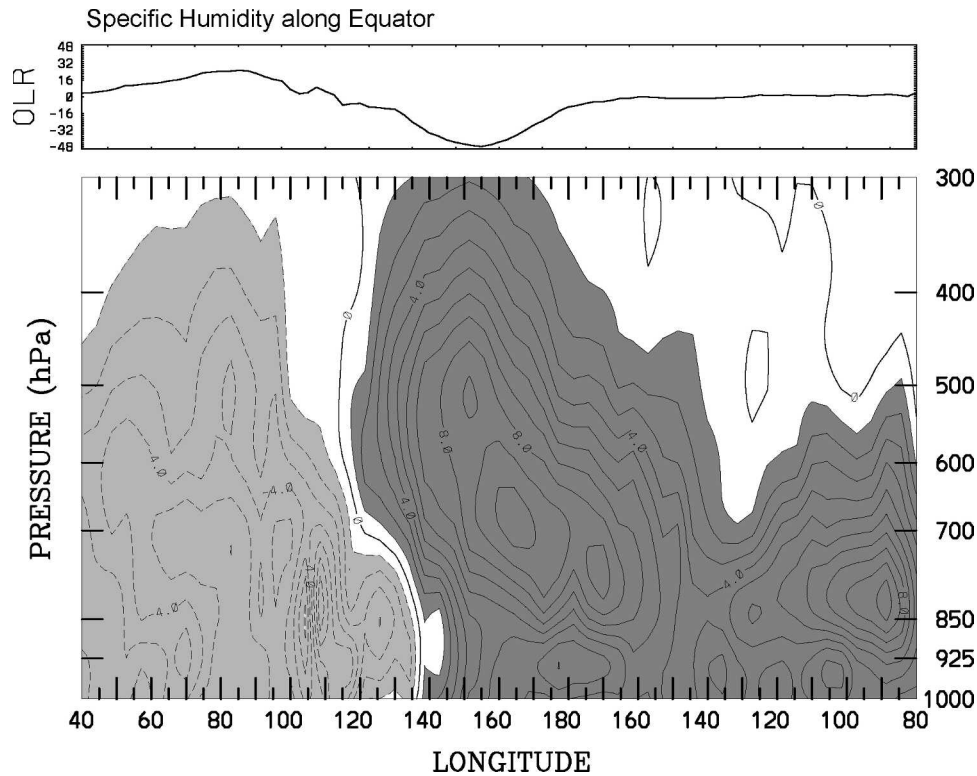


FIG. 9. As in Fig. 3, except for anomalous specific humidity along the equator from 40°E to 80°W. Contour interval is $1 \times 10^{-1} \text{ g kg}^{-1}$.

entire Pacific, the lower troposphere is anomalously moist. This moist layer extends up to 500 hPa to the east of about 130°W, then tilts westward with height back toward the west Pacific, with a peak q' seen at 600 hPa within the convective envelope. Over the Indian sector the entire column is dry in the wake of the disturbance, with a moist upper troposphere and dry lower troposphere over Indonesia.

The divergence and q' patterns of Figs. 5 and 9 imply large-scale moisture convergence in the lower troposphere ahead of the MJO, followed by rapid moistening in the vertical as deep convection develops. Low-level drying initially precedes a more rapid drying of the troposphere to the west of the MJO, a signal in agreement with that found by Kemball-Cook and Weare (2001) using station data and by Seo and Kim (2003) and Sperber (2003) in NCEP reanalysis. This drying would initially occur in convective downdrafts of the stratiform region, with large-scale Rossby gyres behind the MJO bringing subsiding subtropical air into low latitudes through a deep layer. Myers and Waliser (2003) used Television Infrared Observation Satellite (TIROS) Operational Vertical Sounder (TOVS) moisture estimates to examine the structure of q' associated with the MJO and found that low-level humidity leads MJO convec-

tion, but that in general ERA-15 reanalysis as well as TOVS appeared to underestimate the actual value of humidity fluctuations somewhat. Nevertheless both of these studies found evidence that moistening over the Pacific occurred more gradually ahead of the propagating MJO convection than it did within developing MJO convection over the Indian Ocean, where rapid moistening occurred.

These differences are confirmed by a comparison of radiosonde data. At Diego Garcia (Fig. 10a), Medan (Fig. 10b), and Honiara (Fig. 10c), moistening preceding and drying following MJO convection is observed first at 850 hPa, but the vertical propagation of the signal proceeds more rapidly at Diego Garcia, and this also occurs at other stations over the limited sample in the Indian Ocean (Seychelles and Cocos Island; not shown). At stations with higher vertical resolution, such as Truk (Fig. 10d), this initial moistening and drying following is seen to actually be maximized at the 950-hPa level, and this signal is consistent throughout other stations with 50-hPa resolution (not shown), although unfortunately none of these sites are in the Indian or Indonesian sectors for comparison. At Truk, a distinct moist wedge is seen starting at around day -25 at the 950-hPa level sandwiched between still dry air near the

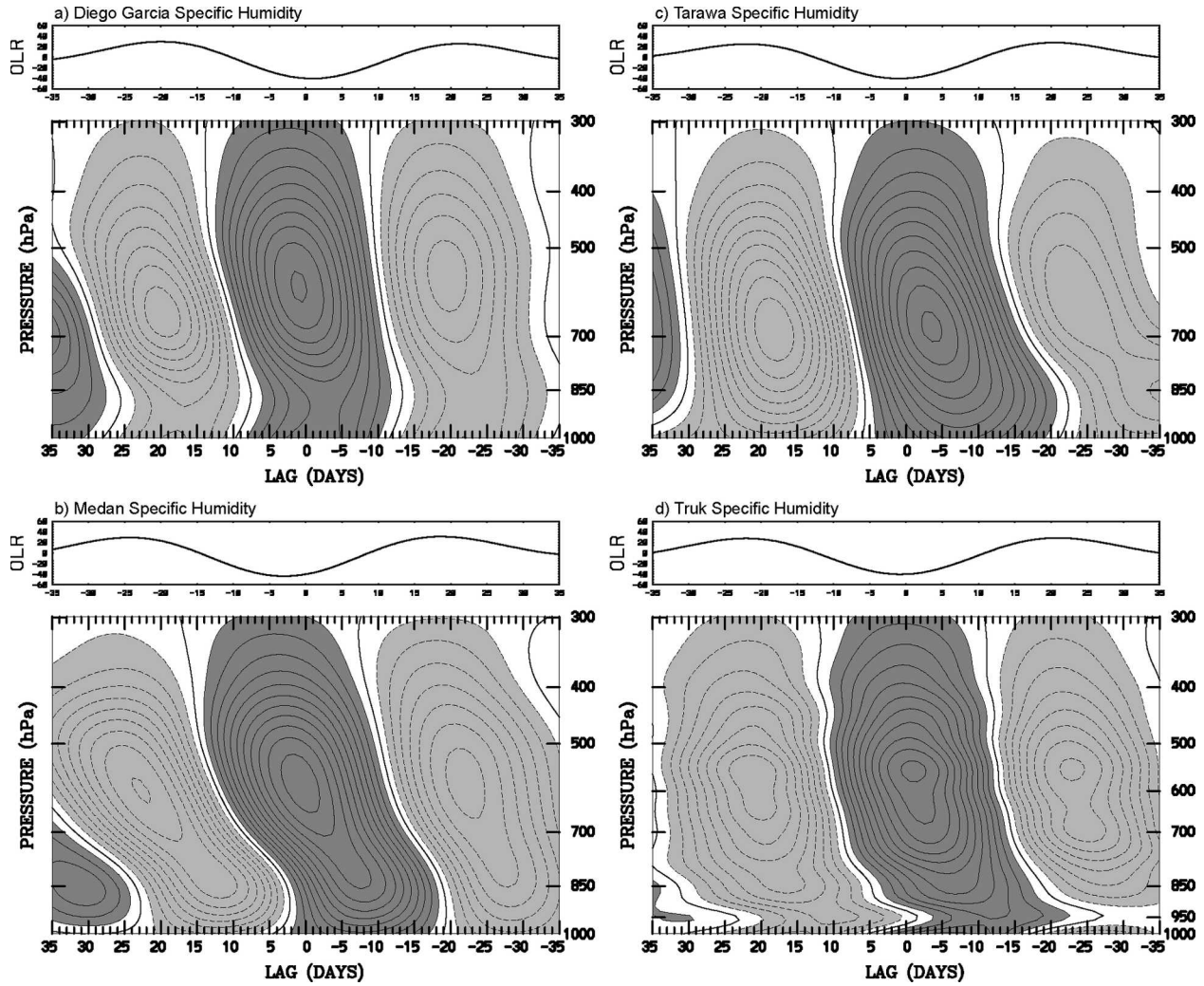


FIG. 10. As in Fig. 4, except for anomalous specific humidity at (a) Diego Garcia, (b) Medan, (c) Tarawa, and (d) Truk. Contour interval is $1 \times 10^{-1} \text{ g kg}^{-1}$.

surface and above. Over several days, this moisture gradually builds vertically, until around day -13 when rapid moistening is seen throughout the column. This progression, along with the drying of the lower troposphere following the deepest convection, is similar to the evolution within tropical mesoscale convective complexes (MCS; e.g., Gamache and Houze 1985), Kelvin waves (Straub and Kiladis 2003b), and two-day waves (Haertel and Kiladis 2004).

As with other fields described above, the phasing between low-level moisture and the convective envelope of the MJO depends substantially on location. Figure 11 plots the near equatorial time–longitude evolution of moisture at 850 hPa, near the level of maximum q' perturbations, from day -35 to $+35$. This field is also a good proxy for the surface equivalent potential temperature, convective available potential energy (CAPE;

see Emanuel 1994), and moist static energy, all of which display very similar phase relationships to OLR. Prior to the development of the MJO in the western Indian Ocean (around day -30 and $+20$) moisture builds in situ to the east of 40°E before it begins eastward propagation ahead of the MJO negative OLR signal. Over the Indian and Indonesian sectors maximum low-level q' remains around $1/8$ of a cycle ahead of the convection, with a phase speed of around 5 m s^{-1} . Once convection reaches the western Pacific on around day -10 , the positive q' signal decouples from the attenuating OLR signal and spreads rapidly eastward across the entire Pacific at around 33 m s^{-1} . This signal is initially blocked by the Andes Mountains at 80°W , followed by a rapid but weaker increase of q' across the Atlantic, which then propagates more slowly across Africa and back into the Indian Ocean at a more typical phase

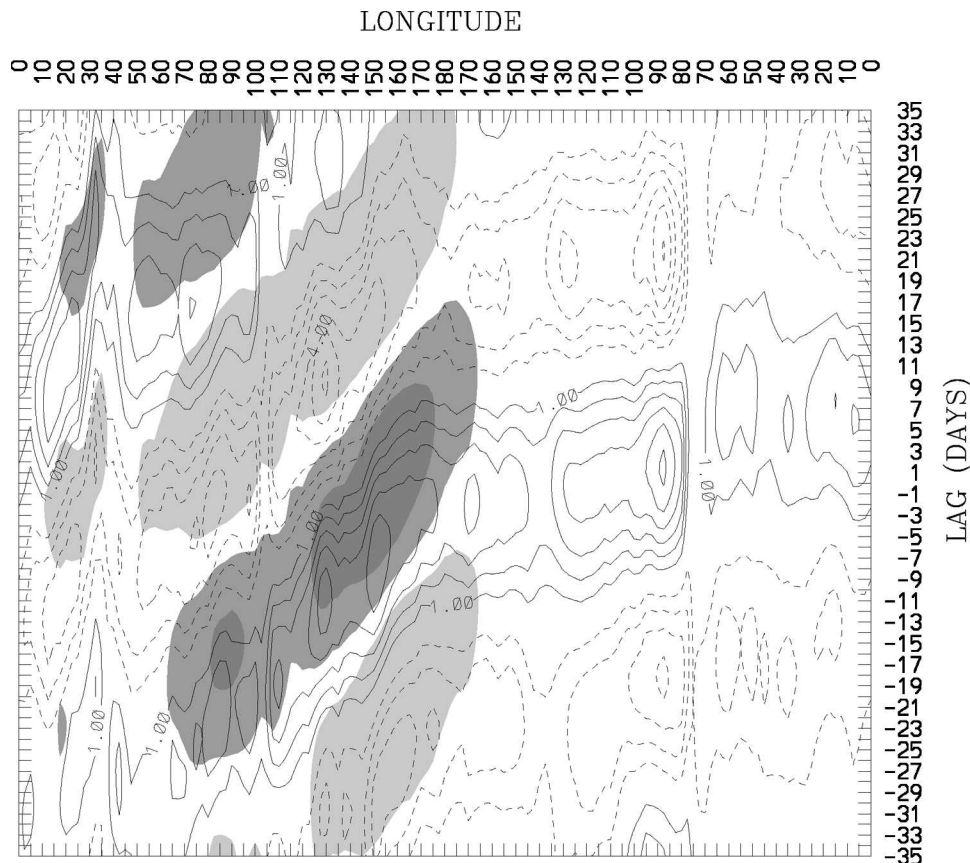


FIG. 11. Time-longitude diagram of anomalous 850-hPa specific humidity (contours, interval is $1 \times 10^{-1} \text{ g kg}^{-1}$, negative dashed) and OLR [shading, dark (darkest) shading denotes OLR anomalies less than -16 W m^{-2} (-18 W m^{-2}), and light shading anomalies greater than $+16 \text{ W m}^{-2}$] from day -35 through day $+35$ averaged from 10°S to 10°N , associated with a -40 W m^{-2} perturbation in MJO-filtered OLR at the $0^{\circ}, 155^{\circ}\text{E}$ on day 0.

speed of 5 m s^{-1} . Rapid eastward propagation of MJO-related signals over the Pacific was observed in the original study of Madden and Julian (1972) and in many studies since (e.g., Hendon and Salby 1994; Bantzer and Wallace 1996; Weickmann et al. 1997; Milliff et al. 1998; Matthews 2000; Sperber 2003). This rapid phase speed is ascribed to a free first baroclinic Kelvin mode emanating from evolving MJO convection over the warm pool (Milliff and Madden 1996; Hendon and Salby 1996), and it has been argued that the continuation of this signal around the globe is a mechanism for the initiation of the next MJO cycle (Matthews 2000; Seo and Kim 2003).

Maps (not shown) and time-longitude plots of q' and divergence (Sperber 2003) reveal a strong local relationship between convergence and anomalously high q' at all lower tropospheric levels over Indian Ocean, but a much weaker relationship over the Pacific. This suggests that moisture flux convergence is crucial for moistening the lower troposphere over the Indian sec-

tor ahead of the MJO, but that local evaporation may be more important over the Pacific (see Weare 2003), where the lower troposphere moistens rapidly but it remains dry above the boundary layer for a longer period prior to convection. This moistening likely occurs as a result of combined weak surface convergence and strong evaporation in the enhanced low-level easterlies that rapidly develop over the Pacific when convection reaches the west Pacific (Fig. 2b), in response to the free Kelvin mode.

e. Diabatic heating

Over a wide range of scales, the heating in convectively coupled equatorial disturbances can be realistically approximated by a two-mode vertical structure (e.g., Mapes and Houze 1995; Mapes 2000; Majda and Shefter 2001; Majda et al. 2004; Haertel and Kiladis 2004). The first mode represents deep convection, with a latent heating maximum in the middle troposphere.

The second mode lags the first by some interval and corresponds to stratiform precipitation, with latent heating confined to the upper troposphere in decks of stratiform clouds, and cooling at lower levels due to subsidence and the evaporation of precipitation through drier air in downdrafts. The superposition of these two modes of precipitation leads to the top-heavy heating profiles typically observed within tropical convective disturbances (e.g., Houze 1989). The leading portion of the second mode can also be profitably envisioned as representing the effects of low-level heating due to shallow convection, associated with low-level convergence and midlevel divergence, and also radiational cooling aloft in subsidence. Although the vertical scales of heating and cooling in shallow convection may not strictly mirror that within stratiform regions, it has been found that the two-mode representation accounts for the bulk of the observed heating during COARE for two-day wave disturbances (e.g., Haertel and Kiladis 2004). In addition to its convenience for use in a simple modeling setting the two-mode approach is physically based and thus appealing.

Observations during COARE showed shallow convection developing into midlevel congestus clouds within the leading portion of the MJO, followed by the buildup of deep convection, and finally stratiform precipitation, which lagged by several days (Johnson et al. 1999; Lin et al. 2004; Kikuchi and Takayabu 2004). Figure 12 shows the vertical decomposition of MJO diabatic heating (Q1) obtained applying the technique of Yanai et al. (1973) to corrected COARE divergence profiles (Ciesielski et al. 2003). Here Q1 was regressed onto 30–96-day filtered brightness temperature, then the vertical mode decomposition approach of Fulton and Schubert (1985) with a rigid lid at 150 hPa was used to obtain the first two vertical modes, which account for almost all of the total heating (see Haertel and Kiladis 2004 for details). The Q1 maximum (Fig. 12a) leads the minimum OLR by several days and, as found by Lin et al. (2004), Q1 peaks at 400 hPa and has a distinct westward tilt with height, which is more pronounced than that implied by the vertical motion in Fig. 6. This tilt results from the superposition of the more vertically oriented heating profiles of the deep convective (Fig. 12b) and stratiform (Fig. 12c) modes. In Fig. 12b deep convective heating is maximized at about day -2 while the upper tropospheric second mode heating peaks closer to day $+8$, and near day -20 in the lower troposphere in Fig. 12c. This evolution compares well with the progression of heating in two-day waves (Haertel and Kiladis 2004), which proceeds at a much faster pace (hours instead of days).

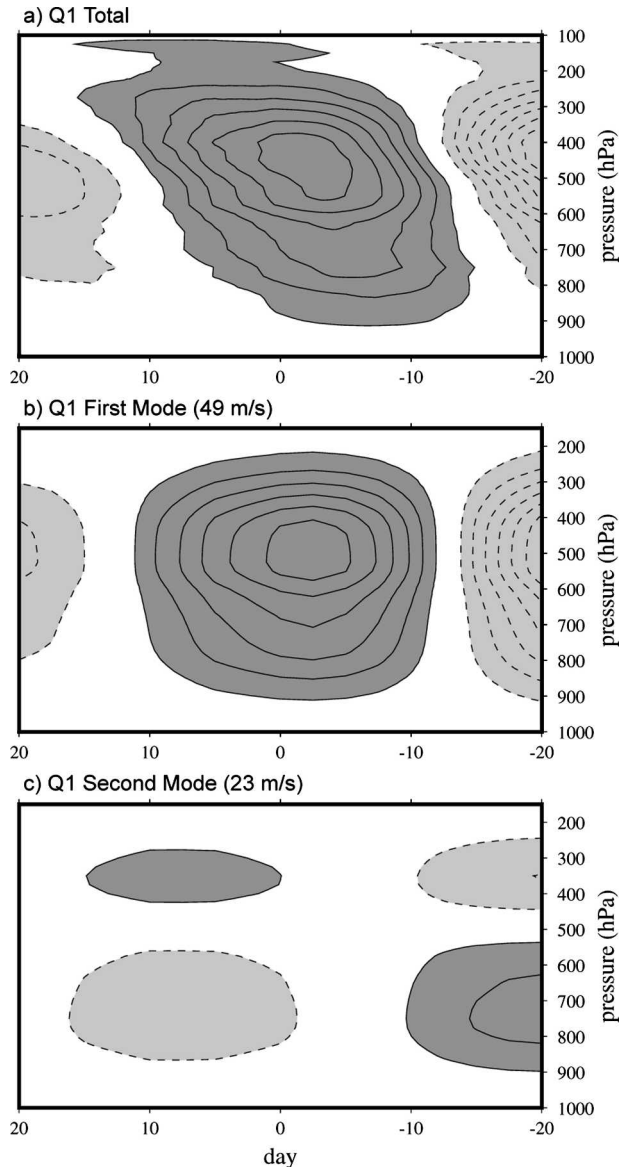


FIG. 12. Time–height diagrams of the perturbation heating (Q1) regressed against MJO-filtered OLR during TOGA COARE (see text for details). (a) Total heating anomaly, (b) first vertical mode, and (c) second vertical mode. Contour interval is $0.5^{\circ}\text{C day}^{-1}$; dark shading is positive.

4. Discussion

Comparing the heating profiles in Fig. 12 to the dynamical structures in Figs. 2–11 leads to the following interpretation of the evolution of the MJO as it propagates eastward over the warm pool. MJO convection is generally preceded by low-level convergence (Fig. 5), moistening (Figs. 9–11), and upward motion in the lower troposphere (Fig. 6), while upper subsidence, cooling, and drying still prevails (e.g., from day -20 to day -15 in Figs. 10b–d and 12). The low-level moist-

ening and accompanying warming due to shortwave radiation and surface fluxes initially result in the destabilization of the boundary layer and the development of shallow convection. This is followed by a gradual lofting of moisture into the middle troposphere by congestus clouds, then a sharp intensification of upward motion and latent heating in the upper tropospheric region of deep convection. After the passage of the heaviest rainfall, the WWB region is accompanied by stratiform precipitation in a region where lower tropospheric subsidence and drying coincide with continuing upper tropospheric moisture and upward motion. This latter signal would occur at around 140°E in Fig. 6, although based on a comparison with COARE data it is likely that ERA-15 does not capture the full extent of the westward tilt of the vertical w' profile implied by Fig. 12, perhaps due in part to the misrepresentation of the stratiform component in model convective parameterizations used to obtain the first-guess analysis (Lin et al. 2004).

Analysis of the statistical evolution of the MJO has revealed distinct differences in the mean structure of the disturbance over the Indian Ocean versus Indonesia and the Pacific. Although not displayed here, these differences are maintained robustly throughout the seasonal cycle, and provide evidence that the nature of the coupling between convection and dynamics within the MJO varies throughout its life cycle. The evolution of these signals presumably reflects changes in vertical heating profiles, phase speed, and/or the basic state that the MJO propagates through.

In particular, higher vertical mode tropospheric temperature structures appear over the Indian sector (Figs. 8a,b), where there is more pronounced mean easterly vertical shear in the basic-state zonal wind. Various theoretical and modeling results support the notion that horizontal and vertical shear should significantly alter the structure of equatorial waves (e.g., Holton 1970, 1971; Lindzen 1971; Boyd 1978; Zhang and Webster 1989; Wang and Xie 1996; Xie and Wang 1996). Wang and Xie (1996) found that stronger easterly shear with height favors higher amplitude baroclinic modal structures in the lower troposphere in equatorial Rossby and MRG modes, with much less pronounced effects on Kelvin waves. Vertical tilts of equatorial waves are also sensitive to boundary layer friction (e.g., Wang and Chen 1989), along with the scale selection, growth rates, and stability of MJO analogs in simple models (Wang 1988, 2005; Wang and Rui 1990; Moskowitz and Bretherton 2000). These potential effects on the MJO need to be investigated more thoroughly.

Despite regional differences, the coincidence between upper tropospheric warmth and upward motion

is seen throughout the life cycle of the MJO, indicative of a disturbance converting available potential energy to kinetic energy (Yanai et al. 2000). More generally, in a dry propagating wave, or in a moist wave that is near statistical equilibrium, that is, where diabatic heating nearly cancels the adiabatic cooling because of ascent (Emanuel et al. 1994), the temperature due to vertical advection would be in quadrature with the heating field, and warm ahead of the region of upward motion. In a linear vertical mode decomposition, this relationship still roughly holds for each mode, so that the observed upward and westward vertical tilt in the midtropospheric temperature signal of convectively coupled waves would result from the superposition of stratiform lagging deep convective heating (Mapes 2000; Majda et al. 2004). This configuration also causes vertical motion and its associated heating field to be in phase with the strong upper tropospheric positive temperature perturbation from the second (stratiform) mode (see Fig. 10 of Haertel and Kiladis 2004).

Vertical tilts of the zonal wind in Figs. 3, 4b, and 4c indicate substantial vertical fluxes of zonal momentum within the MJO (e.g., Moncrieff 2004). Lin et al. (2005) have shown that, over the west Pacific, the advection of perturbation vertical wind shear by the time mean vertical motion and advection of the time mean zonal wind gradient by the perturbation zonal wind are leading terms in balancing the zonal pressure gradient in the zonal momentum budget of the MJO. At lower levels, advection of the meridional zonal wind gradient by the perturbation meridional wind, and subgrid-scale fluxes, become important. These subgrid-scale terms are generally ascribed to convective momentum transports, which partly account for the westerly acceleration of the WWB region following the peak in convection (Houze et al. 2000; Tung and Yanai 2002). The lack of such strong vertical tilts over the Indian Ocean implies a fundamentally different interaction between the basic-state flow and vertical motion within the MJO over that sector.

Interestingly, the vertical structure of the MJO compares favorably in many respects with other propagating convectively coupled equatorial waves studied by Wheeler et al. (2000). In Kelvin waves (Straub and Kiladis 2002), shallow cumulus heating is observed to precede deep convection and then evolve into stratiform rainfall, but this evolution occurs locally at a much more rapid pace than in the MJO, consistent with its faster eastward phase speed of around 15 m s^{-1} . In radiosonde data, westward tilted structures in t' , u' , and q' show similar phasing to the OLR minimum as in the MJO, with a warm, moist boundary layer within easterlies ahead of the wave, followed by a lower tropo-

spheric cooling and drying in westerlies following (see Fig. 5 of Straub and Kiladis 2003b). In the Kelvin wave, upper tropospheric warmth is also coincident with the OLR minimum and implied latent heating.

A westward propagating analogy to the Kelvin wave, with a comparable phase speed, is provided by two-day WIG disturbances during COARE (Haertel and Johnson 1998; Haertel and Kiladis 2004), which have a similar evolution in cloud morphology (Takayabu et al. 1996; Chen et al. 1996). The temperature structure in these disturbances and in Kelvin waves is most like that of the MJO at the Seychelles and Diego Garcia, with deep convection accompanied by a cooling boundary layer, strongest cold t' centers at 600–700 and 100 hPa, and warm t' at 250 hPa [cf. Figs. 8a and 8b with Fig. 10 of Straub and Kiladis (2002); Fig. 5 of Straub and Kiladis (2003b); Fig. 4 of Haertel and Kiladis (2004); and with cross sections in Wheeler et al. (2000)]. In all cases, positive t' in the upper troposphere is in phase with or leading slightly the deepest convection, and is generally skewed such that it is warmer for a longer period ahead of the wave than behind it. The zonal wind fields in these other waves also have much in common with the MJO evolution once differences in spatial scale are accounted for. In addition, initial low-level moistening, followed by rapid moistening of the entire troposphere and then low-level drying in the cool boundary layer are common features. The combined effect of the boundary layer temperature and moisture signals would be to favor the development of convection ahead of the waves and suppress instability behind them through their effect on the moist static energy budget (e.g., Haertel and Kiladis 2004; Hsu et al. 2004).

The fact that the MJO always propagates eastward has led to a number of theoretical models that utilize Kelvin wave dynamics (e.g., Chang 1977; Lau and Peng 1987; Wang 1988, 2005; Neelin and Yu 1994). Despite some common features, one fundamental difference between the MJO and Kelvin waves relates to the relationship between zonal wind and pressure. In observed convectively coupled Kelvin waves, the zonal wind in both the lower and upper troposphere is very close to being in phase with the pressure perturbation (Straub and Kiladis 2002, 2003b), as predicted by linear theory. This relationship also holds for the MJO over the central and eastern Pacific, where its characteristics resemble a free Kelvin mode (Milliff and Madden 1996). However, Lin et al. (2005) point out that where the MJO is strongly coupled to convection, it is a highly viscous disturbance, in that pressure lags the zonal wind by several days, implying the existence of other important terms in the zonal momentum budget, such as large-scale advection and convective momentum trans-

port. As discussed by Emanuel et al. (1994), under the influence of a basic state such damping terms can shift the relationship between pressure (and thus temperature), and vertical motion in a large-scale convectively coupled wave. In the case of the MJO, this shift favors the collocation of latent heating and positive temperature perturbation, leading to wave amplification (Straub and Kiladis 2003b; Lin et al. 2005).

The ubiquity of many salient dynamical features and cloud structures across a broad range of scales in equatorial waves is perhaps surprising, especially in the case of the MJO that has dispersion characteristics that do not correspond to a normal mode of the shallow water equations (Wheeler and Kiladis 1999). This dispersion relationship describes an isolated wave packet with eastward phase but zero group velocity, once again in contrast to the Kelvin wave where phase and group speeds are identical. It is well documented that the MJO envelope is composed of a variety of smaller-scale, higher-frequency disturbances with eastward or westward phase speeds, (e.g., Nakazawa 1988; Hendon and Liebmann 1994; Straub and Kiladis 2003a). Yet these higher-frequency waves themselves are also composed of individual convective disturbances organized down to the MCS scale [see Straub and Kiladis (2002) on Kelvin waves; Chen et al. (1996) and Takayabu et al. (1996) for two-day WIG examples]. One implication is that the larger convective envelopes tend to be composed of more shallow convection along their leading edges, a preponderance of deep convection in their centers, and then stratiform rainfall along their trailing edges, regardless of scale or propagation direction. This is supported statistically by using Tropical Rainfall Measuring Mission (TRMM) Microwave Imager (TMI) data, which estimate convective–stratiform precipitation area coverage (Olson et al. 2001). Figure 13 shows the result of regressing TMI convective fraction against MJO, Kelvin, and MRG-filtered OLR. In the case of the MJO and Kelvin wave, there is a clear bias for the convective fraction to be higher on the eastern side of the OLR envelope, while for the westward propagating MRG wave, this bias is shifted to the west side. The latter shift occurs despite the westward advection of high cloudiness (and thus low OLR) by the basic state that would presumably occur over the warm pool. We note that the displacement of deep convection with respect to the wavelength of the disturbance appears to be less for the MJO and MRG wave than for the Kelvin wave, so it is clear that the degree of skewness is not strictly tied to the scale of the waves.

Figure 13 suggests some level of self-similar organization in convection over a wide range of scales within equatorial waves. While this scale invariance may ulti-

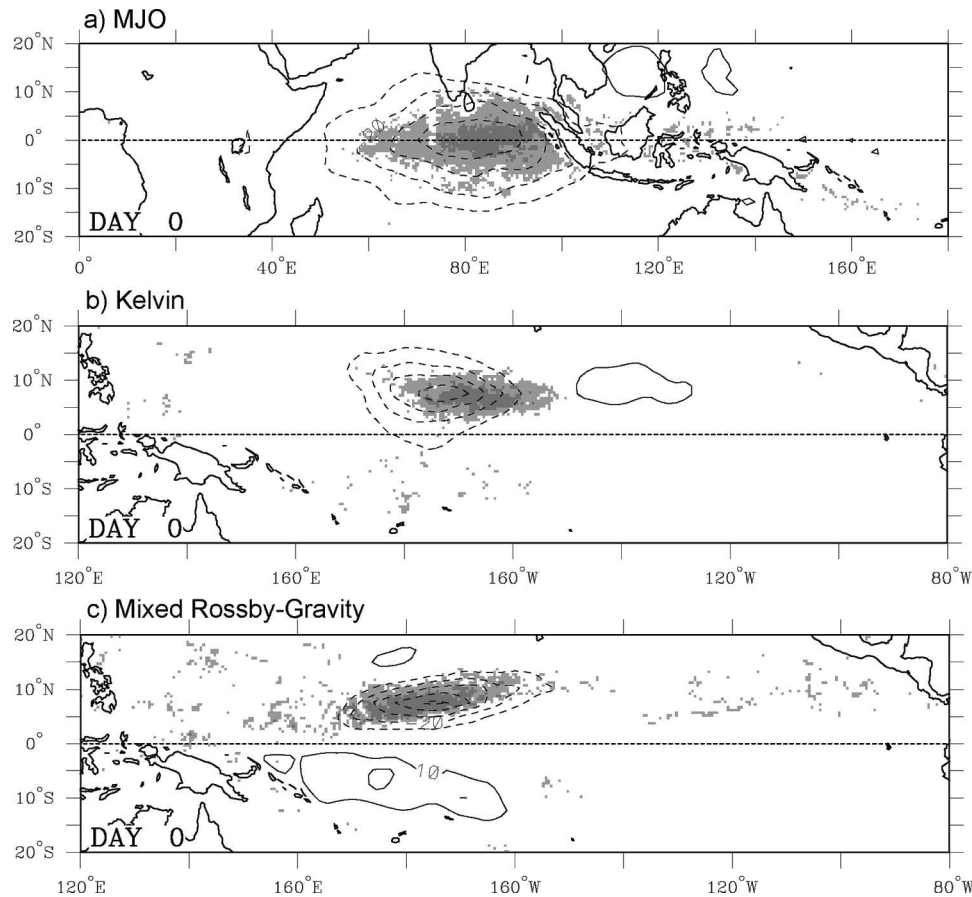


FIG. 13. Percentage of deep convective precipitation regressed against (a) MJO-filtered OLR, (b) Kelvin-filtered OLR, and (c) mixed Rossby-gravity wave filtered OLR. The analysis uses 5 yr of TMI data (see text). OLR contour interval is 10 W m^{-2} , with negative contours dashed. Shaded regions correspond to positive perturbations in deep convection, where the two levels of shading represent anomalies of 2% and 5%. All shaded pixels are significant at the 95% level.

mately be the factor that governs the dynamical similarities across the various wave types, it does raise the question of how the smaller, higher-frequency disturbances that make up the MJO conspire to produce the large-scale heating profile in Fig. 12. It is likely that these individual disturbances all have similar Q1 profiles based on their temperature structures (Wheeler et al. 2000; Straub and Kiladis 2003b), implying that the progression of cloud morphology and heating in these waves is dictated by fundamental interactions with the large-scale circulation (Houze 1989). Whereas a microphysically based argument for the development of stratiform precipitation would lead to a prediction of the development of top-heavy heating within a few hours (e.g., Mapes and Houze 1995), it is remarkable that such a progression is also tied to the scale of individual waves. As a potentially complicating factor to this picture, Mapes and Lin (2005) have found evidence for large geographical differences in inferred heating

profiles in tropical oceanic MCSs. Further progress on understanding the scale interactions between the MJO and other convective disturbances will certainly require more detailed statistical comparisons of their kinematic and thermodynamical structures along with cloud morphology, in conjunction with theoretical and simple modeling studies.

Acknowledgments. We thank Joseph Biello, Andy Majda, Rol Madden, Brian Mapes, Paul Roundy, Masahiro Sugiyama, Baijun Tian, and Bin Wang for stimulating conversations on the MJO and equatorial waves. Insightful comments by Jialin Lin, Charles Warner, Chidong Zhang, and an anonymous reviewer greatly helped to improve the discussion and presentation of the manuscript. This research was supported by NOAA's Office of Global Programs under Grant GC01-351. The CARDS dataset was obtained from NOAA's National Climate Data Center.

REFERENCES

- Bantzer, C. H., and J. M. Wallace, 1996: Intraseasonal variability in tropical mean temperature and precipitation and their relation to the tropical 40–50 day oscillation. *J. Atmos. Sci.*, **53**, 3032–3045.
- Biello, J. A., and A. J. Majda, 2005: A new multiscale model for the Madden–Julian oscillation. *J. Atmos. Sci.*, **62**, 1694–1721.
- Bladé, I., and D. L. Hartmann, 1993: Tropical intraseasonal oscillations in a simple nonlinear model. *J. Atmos. Sci.*, **50**, 2922–2939.
- Boyd, J. P., 1978: The effects of latitudinal shear on equatorial waves. Part I: Theory and methods. *J. Atmos. Sci.*, **35**, 2236–2258.
- Chang, C.-P., 1977: Viscous internal gravity waves and low-frequency oscillations in the Tropics. *J. Atmos. Sci.*, **34**, 901–910.
- , and H. Lim, 1988: Kelvin wave-CISK: A possible mechanism for the 30–50-day oscillation. *J. Atmos. Sci.*, **45**, 1709–1720.
- Chao, W. C., 1987: On the origin of the tropical intraseasonal oscillation. *J. Atmos. Sci.*, **44**, 1940–1949.
- Chen, S. S., R. A. Houze, and B. E. Mapes, 1996: Multiscale variability of deep convection in relation to large-scale circulation in TOGA COARE. *J. Atmos. Sci.*, **53**, 1380–1409.
- Ciesielski, P. E., R. H. Johnson, P. T. Haertel, and J. Wang, 2003: Corrected TOGA COARE sounding humidity data: Impact on diagnosed properties of convection and climate over the warm pool. *J. Climate*, **16**, 2370–2384.
- Dunkerton, T. J., and F. X. Crum, 1995: Eastward propagating ~2- to 15-day equatorial convection and its relation to the tropical intraseasonal oscillation. *J. Geophys. Res.*, **100**, 25 781–25 790.
- Emanuel, K. A., 1987: An air–sea interaction model of intraseasonal oscillations in the Tropics. *J. Atmos. Sci.*, **44**, 2324–2340.
- , 1994: *Atmospheric Convection*. Oxford University Press, 580 pp.
- , J. D. Neelin, and C. S. Bretherton, 1994: On large-scale circulations in convecting atmospheres. *Quart. J. Roy. Meteor. Soc.*, **120**, 1111–1143.
- Flatau, M., P. J. Flatau, P. Phoebus, and P. P. Niiler, 1997: The feedback between equatorial convection and local radiative and evaporative processes: The implications for intraseasonal oscillations. *J. Atmos. Sci.*, **54**, 2373–2386.
- , —, J. Schmidt, and G. N. Kiladis, 2003: Delayed onset of the 2002 Indian monsoon. *Geophys. Res. Lett.*, **30**, 1768, doi:10.1029/2003GL017434.
- Fulton, S. R., and W. H. Schubert, 1985: Vertical normal mode transforms: Theory and application. *Mon. Wea. Rev.*, **113**, 647–658.
- Gamache, J. F., and R. A. Houze, 1985: Further analysis of the composite wind and thermodynamic structure of the 12 September GATE squall line. *Mon. Wea. Rev.*, **113**, 1241–1259.
- Grabowski, W. W., 2003: MJO-like coherent structures: Sensitivity simulations using the cloud-resolving convection parameterization (CRCP). *J. Atmos. Sci.*, **60**, 847–864.
- Gustafson, W. I., and B. C. Weare, 2004: MM5 modeling of the Madden–Julian oscillation in the Indian and west Pacific Oceans: Model description and control run results. *J. Climate*, **17**, 1320–1337.
- Gutzler, D. S., G. N. Kiladis, G. A. Meehl, K. M. Weickmann, and M. Wheeler, 1994: The global climate of December 1992–February 1993. Part II: Large-scale variability across the tropical western Pacific during TOGA COARE. *J. Climate*, **7**, 1606–1622.
- Haertel, P. T., and R. H. Johnson, 1998: Two-day disturbances in the equatorial western Pacific. *Quart. J. Roy. Meteor. Soc.*, **124**, 615–636.
- , and G. N. Kiladis, 2004: On the dynamics of two-day equatorial disturbances. *J. Atmos. Sci.*, **61**, 2707–2721.
- Hayashi, Y., and D. G. Golder, 1993: Tropical 40–50- and 25–30-day oscillations appearing in realistic and idealized GFDL climate models and the ECMWF dataset. *J. Atmos. Sci.*, **50**, 464–494.
- Hendon, H. H., 1988: A simple model of the 40–50 day oscillation. *J. Atmos. Sci.*, **45**, 569–584.
- , and B. Liebmann, 1994: Organization of convection within the Madden–Julian oscillation. *J. Geophys. Res.*, **99**, 8073–8083.
- , and M. L. Salby, 1994: The life cycle of the Madden–Julian oscillation. *J. Atmos. Sci.*, **51**, 2225–2237.
- , and —, 1996: Planetary-scale circulations forced by intraseasonal variations of observed convection. *J. Atmos. Sci.*, **53**, 1751–1758.
- , C. Zhang, and J. D. Glick, 1999: Interannual variation of the Madden–Julian oscillation during austral summer. *J. Climate*, **12**, 2538–2550.
- Holton, J. R., 1970: The influence of mean wind shear on the propagation of Kelvin waves. *Tellus*, **22**, 186–193.
- , 1971: A diagnostic model for equatorial wave disturbances: The role of vertical shear of the mean zonal wind. *J. Atmos. Sci.*, **28**, 55–64.
- Houze, R. A., 1989: Observed structure of mesoscale convective systems and implications for large-scale heating. *Quart. J. Roy. Meteor. Soc.*, **115**, 425–461.
- , S. S. Chen, and D. E. Kingsmill, 2000: Convection over the Pacific warm pool in relation to the atmospheric Kelvin–Rossby wave. *J. Atmos. Sci.*, **57**, 3058–3089.
- Hsu, H.-H., C.-H. Weng, and C.-H. Wu, 2004: Contrasting characteristics between the northward and eastward propagation of the intraseasonal oscillation during the boreal summer. *J. Climate*, **17**, 727–743.
- Hu, Q., and D. A. Randall, 1994: Low-frequency oscillations in radiative–convective systems. *J. Atmos. Sci.*, **51**, 1089–1099.
- Inness, P. M., and J. M. Slingo, 2003: Simulation of the Madden–Julian oscillation in a coupled general circulation model. Part I: Comparison with observations and an atmosphere-only GCM. *J. Climate*, **16**, 345–364.
- Johnson, R. H., T. M. Rickenbach, S. A. Rutledge, P. E. Ciesielski, and W. H. Schubert, 1999: Trimodal characteristics of tropical convection. *J. Climate*, **12**, 2397–2418.
- Jones, C., and B. C. Weare, 1996: The role of low-level moisture convergence and ocean latent heat fluxes in the Madden–Julian oscillation: An observational analysis using ISCCP data and ECMWF analyses. *J. Climate*, **9**, 3086–3140.
- Kemball-Cook, S. R., and B. Wang, 2001: Equatorial waves and air–sea interaction in the boreal summer intraseasonal oscillation. *J. Climate*, **14**, 2923–2942.
- , and B. C. Weare, 2001: The onset of convection in the Madden–Julian oscillation. *J. Climate*, **14**, 780–793.
- Kessler, W. S., 2001: EOF representations of the Madden–Julian Oscillation and its connection with ENSO. *J. Climate*, **14**, 3055–3061.
- Kikuchi, K., and Y. N. Takayabu, 2004: The development of organized convection associated with the MJO during TOGA COARE IOP: Trimodal characteristics. *Geophys. Res. Lett.*, **31**, L10101, doi:10.1029/2004GL019601.

- Kiladis, G. N., and K. M. Weickmann, 1992: Circulation anomalies associated with tropical convection during northern winter. *Mon. Wea. Rev.*, **120**, 1900–1923.
- , G. A. Meehl, and K. M. Weickmann, 1994: Large-scale circulation associated with westerly wind bursts and deep convection over the western equatorial Pacific. *J. Geophys. Res.*, **99**, 18 527–18 544.
- , K. H. Straub, G. C. Reid, and K. S. Gage, 2001: Aspects of interannual and intraseasonal variability of the tropopause and lower stratosphere. *Quart. J. Roy. Meteor. Soc.*, **127**, 1961–1984.
- Krishnamurti, T. N., D. R. Chakraborty, N. Cubukcu, S. Stefanova, and T. S. V. Vijaya Kumar, 2003: A mechanism of the Madden-Julian oscillation based on interactions in the frequency domain. *Quart. J. Roy. Meteor. Soc.*, **129**, 2559–2590.
- Lau, K.-M., and L. Peng, 1987: Origin of low frequency (intraseasonal) oscillations in the tropical atmosphere. Part I: The basic theory. *J. Atmos. Sci.*, **44**, 950–972.
- Liebmann, B., and C. A. Smith, 1996: Description of a complete (interpolated) OLR dataset. *Bull. Amer. Meteor. Soc.*, **77**, 1275–1277.
- Lin, J., B. E. Mapes, M. Zhang, and M. Newman, 2004: Stratiform precipitation, vertical heating profiles, and the Madden-Julian oscillation. *J. Atmos. Sci.*, **61**, 296–309.
- , M. Zhang, and B. E. Mapes, 2005: Zonal momentum budget of the Madden-Julian oscillation: The source and strength of equivalent linear damping. *J. Atmos. Sci.*, **62**, 2172–2188.
- Lin, J. W.-B., J. D. Neelin, and N. Zeng, 2000: Maintenance of tropical intraseasonal variability: Impact of evaporation-wind feedback and midlatitude storms. *J. Atmos. Sci.*, **57**, 2793–2823.
- Lin, X., and R. H. Johnson, 1996: Heating, moistening, and rainfall over the western Pacific warm pool during TOGA COARE. *J. Atmos. Sci.*, **53**, 3367–3383.
- Lindzen, R. S., 1971: Equatorial planetary-scale waves in shear. Part I. *J. Atmos. Sci.*, **28**, 609–622.
- , 2003: The interaction of waves and convection in the Tropics. *J. Atmos. Sci.*, **60**, 3009–3020.
- Livezey, R. E., and W. Y. Chen, 1983: Statistical field significance and its determination by Monte Carlo techniques. *Mon. Wea. Rev.*, **111**, 46–59.
- Madden, R., and P. Julian, 1972: Description of global scale circulation cells in the Tropics with a 40–50 day period. *J. Atmos. Sci.*, **29**, 1109–1123.
- , and —, 2005: Historical perspective. *Intraseasonal Variability in the Atmosphere–Ocean Climate System*, W. K.-M. Lau and D. Waliser, Eds., Springer-Praxis, 1–16.
- Majda, A. J., and M. G. Shefter, 2001: Models for stratiform instability and convectively coupled waves. *J. Atmos. Sci.*, **58**, 1567–1584.
- , and J. A. Biello, 2004: A multiscale model for tropical intraseasonal oscillations. *Proc. Natl. Acad. Sci.*, **101**, 4736–4741.
- , B. Khouider, G. N. Kiladis, K. H. Straub, and M. G. Shefter, 2004: A model for convectively coupled tropical waves: Nonlinearity, rotation, and comparison with observations. *J. Atmos. Sci.*, **61**, 2188–2205.
- Maloney, E. D., and D. L. Hartmann, 1998: Frictional moisture convergence in a composite life cycle of the Madden-Julian oscillation. *J. Climate*, **11**, 2387–2403.
- , and A. H. Sobel, 2004: Surface fluxes and ocean coupling in the tropical intraseasonal oscillation. *J. Climate*, **17**, 4368–4386.
- Mapes, B. E., 2000: Convective inhibition, subgrid-scale triggering energy, and stratiform instability in a toy tropical wave model. *J. Atmos. Sci.*, **57**, 1515–1535.
- , and R. A. Houze, 1993: Cloud clusters and superclusters over the oceanic warm pool. *Mon. Wea. Rev.*, **121**, 1398–1415.
- , and —, 1995: Diabatic divergence profiles in western Pacific mesoscale convective systems. *J. Atmos. Sci.*, **52**, 1807–1828.
- , and J. Lin, 2005: Doppler radar observations of mesoscale wind divergences in regions of tropical convection. *Mon. Wea. Rev.*, **133**, 1808–1824.
- Matthews, A. J., 2000: Propagation mechanisms for the Madden-Julian oscillation. *Quart. J. Roy. Meteor. Soc.*, **126**, 2637–2651.
- , B. J. Hoskins, and M. Masutani, 2004: The global response to tropical heating in the Madden-Julian oscillation during northern winter. *Quart. J. Roy. Meteor. Soc.*, **130**, 1991–2012.
- Meehl, G. A., R. Lukas, G. N. Kiladis, K. M. Weickmann, A. J. Matthews, and M. Wheeler, 2001: A conceptual framework for time and space scale interactions in the climate system. *Climate Dyn.*, **17**, 753–775.
- Milliff, R. F., and R. A. Madden, 1996: The existence and vertical structure of fast, eastward-moving disturbances in the equatorial troposphere. *J. Atmos. Sci.*, **53**, 586–597.
- , T. J. Hoar, and R. A. Madden, 1998: Fast, eastward-moving disturbances in the surface winds of the equatorial Pacific. *Tellus*, **50A**, 26–41.
- Moncrieff, M. W., 2004: Analytic representation of the large-scale organization of tropical convection. *J. Atmos. Sci.*, **61**, 1521–1538.
- Moskowitz, B. M., and C. S. Bretherton, 2000: An analysis of frictional feedback on a moist equatorial Kelvin mode. *J. Atmos. Sci.*, **57**, 2188–2206.
- Mote, P. W., H. L. Clark, T. J. Dunkerton, R. S. Harwood, and H. C. Pumphrey, 2000: Intraseasonal variations of water vapor in the tropical upper troposphere and tropopause region. *J. Geophys. Res.*, **105**, 17 457–17 470.
- Myers, D. S., and D. E. Waliser, 2003: Three-dimensional water vapor and cloud variations associated with the Madden-Julian oscillation during Northern Hemisphere winter. *J. Climate*, **16**, 929–950.
- Nakazawa, T., 1988: Tropical super clusters within intraseasonal variations over the western Pacific. *J. Meteor. Soc. Japan*, **66**, 823–839.
- Neelin, J. D., and J.-Y. Yu, 1994: Modes of tropical variability under convective adjustment and the Madden-Julian oscillation. Part I: Analytical theory. *J. Atmos. Sci.*, **51**, 1876–1894.
- , I. M. Held, and K. H. Cook, 1987: Evaporation-wind feedback and low-frequency variability in the tropical atmosphere. *J. Atmos. Sci.*, **44**, 2341–2348.
- Olson, W. S., Y. Hong, C. D. Kummerow, and J. Turk, 2001: A texture-polarization method for estimating convective-stratiform precipitation are a coverage from passive microwave radiometer data. *J. Appl. Meteor.*, **40**, 1577–1591.
- Randall, D., M. Khairoutdinov, A. Arakawa, and W. Grabowski, 2003: Breaking the cloud parameterization deadlock. *Bull. Amer. Meteor. Soc.*, **84**, 1547–1564.
- Raymond, D. J., 2001: A new model of the Madden-Julian oscillation. *J. Atmos. Sci.*, **58**, 2807–2819.
- Reed, R. J., D. C. Norquist, and E. E. Recker, 1977: The structure and properties of African wave disturbances as observed during Phase III of GATE. *Mon. Wea. Rev.*, **105**, 317–333.
- Roundy, P. E., and W. M. Frank, 2004a: Effects of low-frequency

- wave interactions on intraseasonal oscillations. *J. Atmos. Sci.*, **61**, 3025–3040.
- , and —, 2004b: Applications of a multiple linear regression model to the analysis of relationships between eastward- and westward-moving intraseasonal modes. *J. Atmos. Sci.*, **61**, 3041–3048.
- Rui, H., and B. Wang, 1990: Development characteristics and dynamic structure of tropical intraseasonal convection anomalies. *J. Atmos. Sci.*, **47**, 357–379.
- Salby, M. L., and H. H. Hendon, 1994: Intraseasonal behavior of clouds, winds, and temperature in the Tropics. *J. Atmos. Sci.*, **51**, 2207–2224.
- , R. Garcia, and H. H. Hendon, 1994: Planetary-scale circulations in the presence of climatological and wave-induced heating. *J. Atmos. Sci.*, **51**, 2344–2367.
- Sassi, F., M. Salby, H. C. Pumphrey, and W. G. Read, 2002: Influence of the Madden–Julian oscillation on upper tropospheric humidity. *J. Geophys. Res.*, **107**, 4681, doi:10.1029/2001JD001331.
- Seo, K.-H., and K.-Y. Kim, 2003: Propagation and initiation mechanisms of the Madden–Julian oscillation. *J. Geophys. Res.*, **108**, 4384, doi:10.1029/2002JD002876.
- Sherwood, S. C., and R. Wahrlich, 1999: Observed evolution of tropical deep convective events and their environment. *Mon. Wea. Rev.*, **127**, 1777–1795.
- , T. Horinouchi, and H. A. Zeleznik, 2003: Convective impact on temperatures observed near the tropical tropopause. *J. Atmos. Sci.*, **60**, 1847–1856.
- Shinoda, T., H. H. Hendon, and J. Glick, 1998: Intraseasonal variability of surface fluxes and sea surface temperature in the tropical western Pacific and Indian Oceans. *J. Climate*, **11**, 1685–1702.
- Sperber, K. R., 2003: Propagation and the vertical structure of the Madden–Julian oscillation. *Mon. Wea. Rev.*, **131**, 3018–3037.
- , J. M. Slingo, P. M. Inness, and W. K.-M. Lau, 1997: On the maintenance and initiation of the intraseasonal oscillation in the NCEP/NCAR reanalysis and in the GLA and UKMO AMIP simulations. *Climate Dyn.*, **13**, 769–795.
- Straub, K. H., and G. N. Kiladis, 2002: Observations of a convectively coupled Kelvin wave in the eastern Pacific ITCZ. *J. Atmos. Sci.*, **59**, 30–53.
- , and —, 2003a: Interactions between the boreal summer intraseasonal oscillation and higher frequency tropical wave activity. *Mon. Wea. Rev.*, **131**, 945–960.
- , and —, 2003b: The observed structure of convectively coupled Kelvin waves: Comparison with simple models of coupled wave instability. *J. Atmos. Sci.*, **60**, 1655–1668.
- Takayabu, Y. N., 1994: Large-scale cloud disturbances associated with equatorial waves. Part II: Westward propagating inertio-gravity waves. *J. Meteor. Soc. Japan*, **72**, 451–465.
- , K.-M. Lau, and C.-H. Sui, 1996: Observation of a quasi-2-day wave during TOGA COARE. *Mon. Wea. Rev.*, **124**, 1892–1913.
- Tung, W.-W., and M. Yanai, 2002: Convective momentum transport observed during the TOGA COARE IOP. Part I: General features. *J. Atmos. Sci.*, **59**, 1857–1871.
- Waliser, D. E., C. Jones, J.-K. Schemm, and N. E. Graham, 1999: A statistical extended-range tropical forecast model based on the slow evolution of the Madden–Julian oscillation. *J. Climate*, **12**, 1918–1939.
- Wang, B., 1988: Dynamics of tropical low-frequency waves: An analysis of the moist Kelvin wave. *J. Atmos. Sci.*, **45**, 2051–2065.
- , 2005: Theory. *Intraseasonal Variability in the Atmosphere–Ocean Climate System*, W. K.-M. Lau and D. Waliser, Eds., Springer-Praxis, 307–351.
- , and J. Chen, 1989: On the zonal-scale selection and vertical structure of equatorial intraseasonal waves. *Quart. J. Roy. Meteor. Soc.*, **115**, 1301–1323.
- , and H. Rui, 1990: Dynamics of the moist Kelvin–Rossby wave on an equatorial β -plane. *J. Atmos. Sci.*, **47**, 397–413.
- , and X. Xie, 1996: Low-frequency equatorial waves in vertically sheared zonal flow. Part I: Stable waves. *J. Atmos. Sci.*, **53**, 449–467.
- Wang, W., and M. E. Schlesinger, 1999: The dependence on convection parameterization of the tropical intraseasonal oscillation simulated by the UIUC 11-layer atmospheric GCM. *J. Climate*, **12**, 1423–1457.
- Weare, B. C., 2003: Composite singular value decomposition analysis of moisture variations associated with the Madden–Julian oscillation. *J. Climate*, **16**, 3779–3792.
- Weickmann, K. M., 1983: Intraseasonal circulation and outgoing longwave radiation modes during Northern Hemisphere winter. *Mon. Wea. Rev.*, **111**, 1838–1858.
- , G. R. Lussy, and J. E. Kutzbach, 1985: Intraseasonal (30–60 day) fluctuations of outgoing longwave radiation and 250 mb streamfunction during northern winter. *Mon. Wea. Rev.*, **113**, 941–961.
- , G. N. Kiladis, and P. D. Sardeshmukh, 1997: The dynamics of intraseasonal atmospheric angular momentum oscillations. *J. Atmos. Sci.*, **54**, 1445–1461.
- Wheeler, M. C., and H. H. Hendon, 2004: An all-season real-time multivariate MJO index: Development of an index for monitoring and prediction. *Mon. Wea. Rev.*, **132**, 1917–1932.
- , and G. N. Kiladis, 1999: Convectively coupled equatorial waves: Analysis of clouds in the wavenumber–frequency domain. *J. Atmos. Sci.*, **56**, 374–399.
- , —, and P. J. Webster, 2000: Large-scale dynamical fields associated with convectively coupled equatorial waves. *J. Atmos. Sci.*, **57**, 613–640.
- Woolnough, S. J., J. M. Slingo, and B. J. Hoskins, 2000: The relationship between convection and sea surface temperature on intraseasonal time scales. *J. Climate*, **13**, 2086–2104.
- Xie, X., and B. Wang, 1996: Low-frequency equatorial waves in vertically sheared zonal flow. Part II: Unstable waves. *J. Atmos. Sci.*, **53**, 3589–3605.
- Yanai, M., S. Esbensen, and J. Chu, 1973: Determination of bulk properties of tropical cloud clusters from large-scale heat and moisture budgets. *J. Atmos. Sci.*, **30**, 611–627.
- , B. Chen, and W.-W. Tung, 2000: The Madden–Julian oscillation observed during the TOGA COARE IOP: Global view. *J. Atmos. Sci.*, **57**, 2374–2396.
- Zhang, C., 1996: Atmospheric intraseasonal variability at the surface in the tropical western Pacific Ocean. *J. Atmos. Sci.*, **53**, 739–758.
- , 2005: The Madden–Julian oscillation. *Rev. Geophys.*, in press.
- , and P. J. Webster, 1989: Effects of zonal flows on equatorially trapped waves. *J. Atmos. Sci.*, **46**, 3632–3652.
- , and M. J. McPhaden, 2000: Intraseasonal surface cooling in the equatorial western Pacific. *J. Climate*, **13**, 2261–2276.
- , and S. P. Anderson, 2003: Sensitivity of intraseasonal perturbation in SST to the structure of the MJO. *J. Atmos. Sci.*, **60**, 2196–2207.
- , and M. Dong, 2004: Seasonality in the Madden–Julian oscillation. *J. Climate*, **17**, 3169–3180.